https://doi.org/10.1016/j.energy.2020.118958

Sulfur-tolerant Fe-doped $La_{0.3}Sr_{0.7}TiO_3$ perovskite as anode of direct carbon solid oxide fuel cells

Weizi Cai[a,b], Dan Cao[b], Mingyang Zhou[b], Xiaomin Yan[b], Yuzhi Li[a], Zhen Wu[c], Shengping Lü[a], Caiyun Mao[a], Yongmin Xie[c], Caiwen Zhao[a], Jialing Yu[a], Meng Ni[d], Jiang Liu[b,*],Hailin Wang[a,**]

[a] College of Engineering, South China Agricultural University, Guangzhou 510640, PR China;

[b] Guangzhou Key Laboratory for Surface Chemistry of Energy Materials, New Energy Research Institute, School of Environment and Energy, South China University of Technology, Guangzhou 510006, PR China;

[c] School of Metallurgy and Chemical Engineering，Jiangxi University of Science and Technology，Ganzhou 341000, PR China

[d] Building Energy Research Group, Department of Building and Real Estate, The Hong Kong Polytechnic University, Hung Hom, Kowloon, Hong Kong 999077, PR China.

Abstract

Fe-doped $La_{0.3}Sr_{0.7}TiO_3$ (LSFT) is synthesized and systematically characterized towards application as an anode material for direct carbon solid oxide fuel cells (DC-SOFCs). The structural, electrical and electrochemical properties of LSFT under the

operation conditions of DC-SOFCs have been evaluated. High structural stability, improved ionic conductivity, electrocatalytic activity, and electrochemical performance are demonstrated. Electrolyte-supported DC-SOFC with LSFT anode provides a maximum power density of 292 mW cm^{-2} at 850 °C, which is comparable to those state-of-the-art Ni-YSZ anode for DC-SOFC. In addition, it shows excellent long-term operational stability (over 110 h) in H_2S-containing CO atmosphere. It thus promises as a novel anode candidate for DC-SOFCs with whole-solid-state configuration.

Keywords Direct carbon solid oxide fuel cell; anode catalyst; electrochemical oxidation; Lanthanum doped strontium titanate

1. Introduction

Direct carbon solid oxide fuel cell (DC-SOFC) is a whole-solid-state fuel cell, with a ceramic oxygen ion conductor as electrolyte, operating directly on solid carbon as fuel [1-5]. DC-SOFC is able to offer the highest efficiency of any fuel cell type at near 100% theoretical efficiency at wide temperature range, because of the entropy change of the overall reaction [6]. It has been reported that the fuel utilization efficiency for direct carbon fuel cell is around 80% [7]. Moreover, the overall system efficiencies, including system auxiliary losses, of above 60-70% have been projected. Fifty percent of CO_2 emissions savings can be obtained by using coal fuel cells instead of

conventional coal boilers or coal gasification in power plants [7]. Different from other fuel cells, DC-SOFCs are able to generate electricity without any liquid medium or feeding gas, which avoid leakage and corrosion issues of high temperature liquid medium, simplify system deployment and administration, and reduce overall cost [8-10]. The electrode reactions of DC-SOFC are:

anodic reaction: $C + 2O^{2-} \rightarrow CO_2 + 4e^-$ (1)

cathodic reaction: $O_2 + 4e^- \rightarrow 2O^{2-}$ (2)

Therefore, the overall reaction of DC-SOFC is:

$$C + O_2 \rightarrow CO_2 \quad (3)$$

The first DC-SOFC without any liquid medium was designed by Nakagawa and Ishida in 1988 [11]. They believed that the anodic reaction of DC-SOFC was consisted of the electrochemical reaction of CO (4) and the Boudouard reaction (5):

$$CO + O^{2-} \rightarrow CO_2 + 2e^- \quad (4)$$

$$C + CO_2 \rightarrow 2CO \quad (5)$$

It had been verified by our group, through comparing the electrical performances and impedance spectra of an SOFC operated at carbon and CO, respectively [12]. In the instant of DC-SOFC startup, CO dominates the equilibrium gas composition in the anode chamber of the DC-SOFC, as CO is the favored product in a C-O system with excess carbon at high temperature of DC-SOFC operation. With the discharge of the DC-SOFC, CO firstly takes electrochemical reaction with O^{2-} on the anode of the DC-SOFC, and produces two electrons and CO_2 (Reaction 4). Spontaneously, the product, CO_2, would

diffuse from the anode to the carbon fuel because of the concentration difference, and reacts with carbon to produce more CO (Reaction 5). Then, partial CO would diffuse back to the anode, while the other CO would be released from the system [13]. During the whole process, CO and CO_2 can be perceived as vehicles, delivering the static solid carbon to the DC-SOFC. From another perspective, this process also can be regarded as dry gasification of solid carbon without steam, which skillfully solves the mass transfer issues of solid carbon fuel. Discharge without necessary for carbon fuel to have any physical or chemical contact with the anode of the cell is the most significant feature and superiority to other types of direct carbon fuel cells. In conclusion, the output performance of DC-SOFC is directly affected by the electrochemical reaction of CO (4) and the Boudouard reaction (5).

Accordingly, the strategies for improving the output performance of DC-SOFC should be focused on catalyzing both of reaction (4) and (5). Tang et al. had tried to apply catalysts to promote the electrochemical reaction and Boudouard reaction of DC-SOFCs and successfully improved the performance [3]. Silver-Gadolinium doped ceria (GDC, $Gd_{0.2}Ce_{0.8}O_{1.9}$) composed anode material was applied to catalyze the electrochemical reaction of CO and Fe was loaded on activated carbon fuel to catalyze the Boudouard reaction, respectively. It effectively enhanced the output performance of DC-SOFC from a maximum power density of 4 mW cm^{-2} to 46 mW cm^{-2} at 800 °C. In fact, the Boudouard reaction catalysts have been widely studied for decades. Apart from Fe-based catalysts, other transition metals, alkali metals and alkaline-earth metals also have been developed

as Boudouard reaction catalysts, like Li, K, Ca, Ni and so on [14-16]. Hence, the promoted effects of these Boudouard reaction catalysts on the DCFC performance are investigated systematically. Nevertheless, the studies on the anode catalysts for the electrochemical oxidation of CO for DC-SOFC are still too few to provide a desirable output performance, comparing to that of the conventional hydrogen SOFC (>1000 mW/cm^2 at 800 °C). Therefore, studying and designing an anode material with excellent electrocatalytic activity for electrochemical oxidation of CO is one of the major critical scientific challenges for DC-SOFCs. Moreover, common requirements for an anode of SOFC are applicable for that of DC-SOFC, such as adequate electronic and ionic conductivity, thermal expansion compatibility, high porosity and capacity to prevent coke and resist sulfur.

As the most widely used traditional anode of SOFC, Ni-YSZ had been applied as the anode of a DC-SOFC stack with a configuration of three cells in series [2]. Powered by 5 wt. % Fe-loaded activated carbon fuel, the DC-SOFC stack with a total effective area of 5.4 cm^2 offered an open circuit voltage of 3 V and a peak power of 2.4 W. Infiltrating Cu particles on the Ni-YSZ surface, Dudek et al. found that the DC-SOFC with Cu-Ni-YSZ anode performed better than that with Ni-YSZ anode [17]. The maximum power density of 118 mW cm^{-2} was reached for DC-SOFC with Cu-Ni-YSZ anode at 800 °C, comparing to 96 mW cm^{-2} obtained by DC-SOFC with Ni-YSZ anode. Besides metal-based anode, perovskite material also had been developed as an anode for DC-SOFC. Xiao et al. investigated the electrocatalytic activity of $SrFe_{0.75}Mo_{0.25}O_3$-

$La_{0.9}Sr_{0.1}Ga_{0.8}Mg_{0.2}O_3$ composed anode and the output performance of the corresponding DC-SOFC (405 mW cm^{-2}, 850 °C), which is comparable to that of a Ni-based DC-SOFC[18]. Recently, Lü et al. studied a Nb-doped $La_{0.8}Sr_{0.2}FeO_3$ perovskite oxide as anode of DC-SOFC fueled by activated carbon and corn straw derived carbon [19]. The DC-SOFCs with Nb-doped $La_{0.8}Sr_{0.2}FeO_3$ anode demonstrated peak power densities of 302.8 mW cm^{-2} and 218.5 mW cm^{-2}, when fueled by activated carbon and corn straw carbon at 850 °C, respectively. However, few of the researchers focused on the sulfur tolerance of the anode materials. For coal fuel, the sulfur content generally reaches 0.4- 5 wt. %, which is mortal for a Ni-based anode DC-SOFC. Therefore, development of a DC-SOFC anode material with high catalytic activity and sulfur resistance is meaningful for the practical application of DC-SOFC.

Lanthanum doped strontium titanate (LST), a mixed ionic electronic conducting perovskite oxide, had been reported as the anode of SOFC operated on H_2S-containing hydrogen or H_2S-containing methane with high sulfur tolerance, excellent carbon resistance and acceptable output performance [20-25]. Doping small amount of hetero-ion in the B-site or creating proper A-site deficient of LST were found to be feasible strategies to improve the electrocatalytic activity of LST and the output performance of the corresponding cell, due to the enhanced electronic and ionic conductivity and the reduced polarization resistance [26-33]. Cobalt doped lanthanum strontium titanate was investigated as a potential anode in DC-SOFC by Kulkarni et al. [34]. Fueled by solid carbon, a DC-SOFC with cobalt doped LST anode gave much better performance (25

mW cm^{-2}, 800 °C) than that with LST anode (6 mW cm^{-2}, 800 °C), which was attributed to the improved ionic conductivity by the authors. Nevertheless, the detailed knowledge about the structural and electrochemical properties of LST based perovskite materials as an anode of DC-SOFC is still lacking in the literature.

In this work, a Fe-doped LST perovskite oxide was synthesized and systematically characterized towards the application as the anode electrode for DC-SOFCs. The detailed structure, electrochemical properties and operation stability of iron doped LST was specifically investigated, which was hoped to be able to address the critical scientific challenges of DC-SOFCs.

2. Experimental

2.1. Materials preparation

The anode material of $La_{0.3}Sr_{0.7}Fe_{0.1}Ti_{0.9}O_3$ (LSFT) was synthesized via glycine-nitrate combustion method. Stoichiometric amounts of $La(NO_3)_3 \cdot 6H_2O$, $Sr(NO_3)_2$ and $Fe(NO_3)_3 \cdot 9H_2O$ were used as the source materials and dissolved in deionized water under stirring. According to the stoichiometry of LSFT, tetrabutyl titanate was mixed with the nitrate solutions under agitation, following by adding glycine into the mixed solution with a molar ratio of 1:1 for glycine-cation. Then, the mixtures were heated at 400 °C under stirring using a magnetic stirring heater until the water of the mixtures was evaporated and self-ignition happened. The precursor powders were calcined at 1100 °C for 10 hours in air to obtain pure perovskite phase.

Yttrium stabilized zirconia, (YSZ, Tosoh Corporation, Japan), $(La_{0.60}Sr_{0.40})_{0.95}Co_{0.20}Fe_{0.80}O_{3-\delta}$ (LSCF-P, Fuel Cell Materials Inc., USA), and $Gd_{0.1}Ce_{0.9}O_{2-\delta}$ (GDC10-HP, Fuel Cell Materials Inc., USA) were directly used as electrolyte material and composed cathode materials, respectively.

For the carbon fuel, Ca-loaded activated carbon had been demonstrated as an excellent carbon fuel for a DC-SOFC. Therefore, in this work, Ca-loaded activated carbon was chosen as carbon fuel and prepared using impregnation method, as has been reported elsewhere [16]. To prepare 5 wt. % Ca-loaded carbon fuel, 2.95 g of $Ca(NO_3)_2 \cdot 4H_2O$ was dissolved in deionized water. Then, 10 g of pure activated carbon powder was added into the $Ca(NO_3)_2$ solution under stirring for 1 hour, followed by heat treatment at 80 °C till the solvent was evaporated. Finally, the carbon fuel was heated at 700 °C for 1 hour under N_2 atmosphere to decompose the nitrate.

2.2. Symmetric cell and fuel cell fabrication

The symmetric cells and single cells studies in this work were YSZ electrolyte supported cells, and the electrodes were prepared by spray deposition technique [35]. YSZ electrolyte substrates were fabricated by dry-pressing YSZ powder uniaxially under 200 MPa, followed by sintering at 1400 °C for 4 hours. After heat treatment, the thickness of the YSZ electrolyte was about 200 μm with a diameter of about 11 mm. To increase the oxygen ionic conductivity of the anode, LST and LSFT were mixed with equivalent GDC powders to get LST/LSFT-GDC composed anode. Glycol, ethylene

glycol and isopropyl alcohol were premixed with the electrodes powders (50 wt.% LSFT/LST- 50 wt.% GDC), using a high-energy ball grinder (Fritsch, Pulverisette 6) at a rotational speed of 400 rpm for 30 min to obtain an uniform colloidal suspension, which was then deposited on both sides of the YSZ electrolyte pellets by a spray gun. Finally, the cells were fired at 1000 °C in air for 4 hours to obtain LSFT-GDC/YSZ/LSFT-GDC and LST-GDC/YSZ/LST-GDC symmetrical cells. For single cell with the LSFT/LSFT-GDC/YSZ/LSCF-GDC configuration, the composed cathode suspension (40%LSCF-60%GDC) was deposited on the other side of the YSZ pellets via spray deposition technique and fired at 900 °C in air for 2 hours, after the anode was deposited on one side of the YSZ pellets and heat treatment. The effective surface area of the cathode was 0.28 cm^2.

2.3. Material characterization

An X-ray diffractometer (XRD, Rigaku D/max-IIIA diffractometer, Japan, Cu-Ka radiation, operated at 35 kV, 30 mA, l = 1.54184 Å) was employed to confirm the crystalline structures of sample. The step scanning of the diffraction data was in the 2θ range of 20-80˚ with intervals of 0.02˚. GSAS software was used for Rietveld refinements on the diffraction patterns. Cold field scanning electron microscope (SEM, Hitachi SU8010), scanning transmission electron microscope (STEM, JEOL JEM-2100F) equipped with energy-dispersive X-ray (EDX), and X-ray photospectroscopy (XPS, Escalab 250, Al Kα) were used to observe the microstructures and chemical

compositions of the specimens. Electronic conductivities of the anode materials were measured through a four-probe DC technique in a CO-CO_2 mixed gases atmosphere (95 % CO, 5 % CO_2) within the temperature range of 400-850 °C at intervals of 50 °C. It was carried out with a bar-shaped sample with 2.5×5×12 mm dimensions, which had been sintered at 1400 °C for 4 hours. Ionic conductivities of the anode materials were also measured by electron-blocking method [36] in CO-CO_2 mixed gases within the temperature range of 400-850 °C at intervals of 50 °C. LST or LSFT pellet, sintered at 1400 °C, was plastered onto a YSZ electrolyte pellets with Pt paste. Then, silver paste (DAD-87, 80 wt. % Ag, Shanghai Research Institute of Synthetic Resins, Shanghai, China) was painted on both sides of LST and YSZ as current collectors, following by heat in an oven at 150 °C.

2.4. Cell assembling and characterization

Single cells were sealed to one end of a quartz tube with silver paste for fuel cells test. Silver wires were attached to the anode and cathode, and connected to a Solartron 1287 potentiostat and a Solartron 1260 frequency response analyzer over the temperature range of 750–850 °C. Impedance spectra were acquired under open circuit voltage (OCV) conditions in a frequency range from 0.1 MHz to 0.1 Hz with an AC amplitude of 10 mV. For the cells operated on humidified hydrogen or H_2S-containing carbon monoxide (H_2S, 1000 ppm), the flow rate of fuel gases was 40 mL min^{-1}. For the cells operated on carbon fuel, 0.4 g carbon was filled into each cell. In all the testing

experiment, the cathode side of the cells was exposed to ambient air.

3. Results and discussion

3.1. Phase identification and microstructure of the anode materials

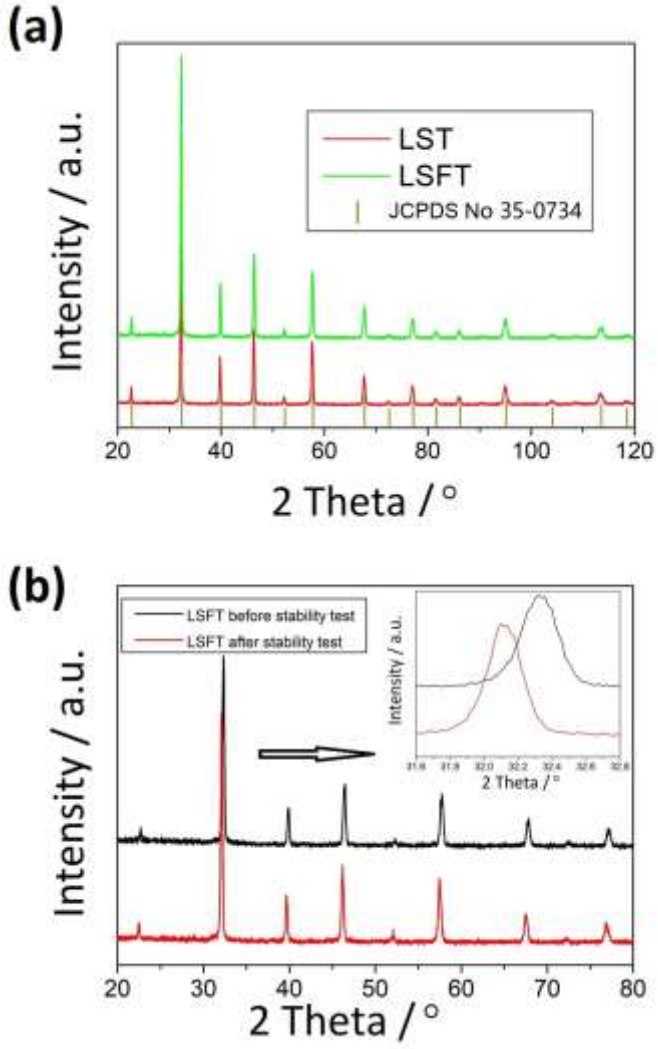

Fig. 1. (a)XRD patterns of the as-prepared LST and LSFT powders and XRD patterns (b) of LST before and after long term stability test.

Table 1
XRD data of as-prepared LSFT.

	Crystal system	Space group	Crystalline domain size	Lattice spacing of (110) plane
LSFT	face-centered cubic	$Pm\bar{3}m$	$a=b=c=$ 3.9119 Å	2.766 Å

Fig. 1(a) shows the XRD patterns of the as-prepared LST and LSFT samples at room temperature, which match those of the standard $SrTiO_3$ perovskite structure (JCPDS No. 35-0734). No other peaks can be observed, indicating high purity of the as-prepared LST and LSFT samples, and the successfully doping of Fe into the B-site of LST perovskite structure. To further confirm the structural information of LSFT, the XRD patterns are analyzed by Rietveld refinement (Figure S1). The phase structure of the as-prepared LSFT can be determined to be a face-centered cubic perovskite structure with a space group of $Pm\bar{3}m$ ($a=b=c=$ 3.9119 Å). The reliability factors (R_{wp} = 7.58 %, R_p = 5.94 %, gof = 1.266) of the Rietveld refinement is low and indicate the good fitting between the calculated and experimental XRD patterns. There is not significantly diffraction angle movement of the peaks of LSFT sample, comparing to that of LST sample, which might because the ionic radii of B-site doping ion, Fe^{3+} (high spin state, 0.0645 nm) is close to that of Ti^{3+} (0.067 nm). In addition, in order to identify the chemical stability of LSFT under the operation condition of DC-SOFC, a LSFT sample is heated at 850 °C (the operation temperature of DC-SOFC) for 48 hours under a CO-CO_2 mixed gases atmosphere (95 % CO, 5 % CO_2) to simulate the anode

atmosphere of DC-SOFC under discharging conditions. The anode atmosphere of DC-SOFC under discharging condition has been confirmed in previous work [37]. Apparently, the XRD pattern of LSFT after long term stability test (Fig. 1b) is similarly to that before long term stability test, and there are no any impurity peaks can be observed, which proves the good chemical stability of LSFT under DC-SOFC operation condition. At the same time, no exsolution of B-site transition metal (Fe) from the lattice of LSFT can be detected after this long-term stability test, which is consistent to the result of Kulkarni et. al.[34]. An exsolution of metal Fe in nanoparticle form on the surface of the perovskite matrix might be interesting. However, in our case, no exsolution of metal Fe can be attributed to the matched ionic radii of Fe^{3+} and Ti^{3+}, the good stability of LSFT perovskite structure and the relatively weak reducing activity of CO-CO_2 mixed gases. What's interesting, we find a slight movement to lower diffraction angle of LSFT after long term stability test, which is shown in the magnified view of the main peaks of LSFT samples at the right corner of Fig. 1(b). Similar result also has been reported by Liu and Luo [38]. This phenomenon can be attributed to the following reasons. Firstly, under a reduction condition, parts of Ti^{4+} and Fe^{3+} of LSFT could be reduced to Ti^{3+} and Fe^{2+}, respectively. The ionic radii of Ti^{3+} and Fe^{2+} are larger than that of Ti^{4+} and Fe^{3+}, respectively. Therefore, a larger B-site ionic would result in an increased lattice parameter and an increased interplanar distance of perovskite material. Secondly, a reduction atmosphere would significantly enhance the oxygen vacancy concentration, and further lead to a lattice expansion of perovskite

material.

For perovskite structure materials, Goldschmidt tolerance factor (t) is regularly applied to define the stability of perovskite structure, which can be expressed as the following equation:

$$t = (r_A+r_O)/(\sqrt{2}(r_B+r_O))$$

Where r_A, r_B and r_O are the radii of the A-site cation, B-site cation, and oxygen ion, respectively. Tolerance factor (t) is widely used to estimate the stability of perovskite materials. If the tolerance factor (t) of the perovskite material is in the range of $0.75 \leq t \leq 1.0$, the perovskite material could be stable. What's more, the closer the tolerance factor (t) is to 1, the more stable the material is. Here, if we hypothesize there is 70 % of Ti^{4+} and 30 % of Ti^{3+} in LST, the oxidation state and spin state of iron ion in LSFT are +3 and high spin state, respectively. Then, t of LST and LSFT are calculated to be 0.9907 and 0.9918, respectively. Both of the t values are in the range of $0.75 \leq t \leq 1.0$, indicating the stability of LST and LSFT perovskite structure. Moreover, the tolerance factor of LSFT even slightly closer to 1 than that of LST, indicating that the stability of LSFT maybe even better than that of LST or as good as LST. It should be noted that the above calculation is based on low temperature and the cubic perovskite structure of LST and LSFT could change during high temperature. Although we have compared the XRD patterns of LSFT before and after stability test, the structure of LSFT during high temperature remains unknown, and an *in-situ* XRD test might need to applied to demonstrate the structure of LSFT at high temperature. In addition, a new

tolerance factor proposed by Bartel et al. has been proven to correctly predicts 92% of compounds as perovskite [39]. Therefore, it is also applied to predict the structure stability of LST and LSFT. The new tolerance factor (τ) has the form:

$$\tau = \frac{r_O}{r_B} - n_A\left(n_A - \frac{{}^{r_A}/_{r_B}}{\ln({}^{r_A}/_{r_B})}\right)$$

Where n_A is the oxidation state of A, r is the ionic radius of ion, and $\tau < 4.18$ indicates perovskite. Here, we also hypothesize there is 70 % of Ti^{4+} and 30 % of Ti^{3+} in LST, the oxidation state and spin state of iron ion in LSFT are +3 and high spin state, respectively. Then, τ of LST and LSFT are calculated to be 3.948 and 3.955, respectively. Both of the τ values are smaller than 4.18, indicating the stability of LST and LSFT perovskite structure.

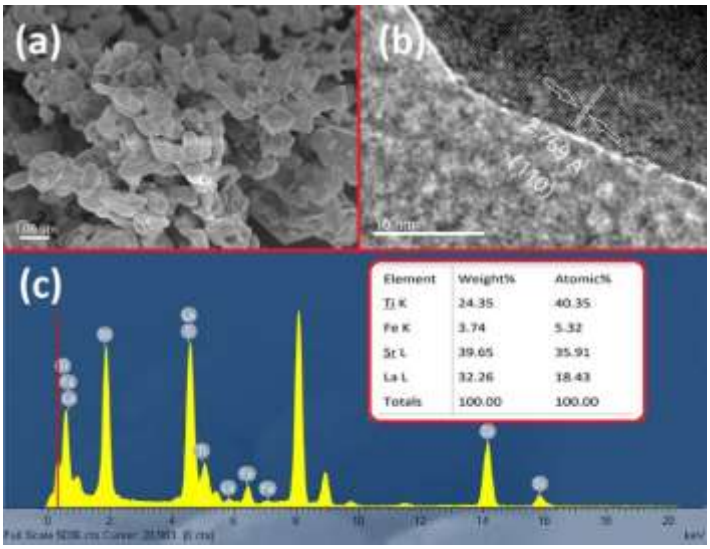

Fig. 2. (a)SEM image, (b)TEM image and (c)EDX results of LSFT.

Fig. 2(a) is an SEM picture of LSFT powder, showing that the average particle

size of LSFT is about 0.5-2.0 um, and the surface of the LSFT particle is smooth without metal Fe nanoparticle exsolution. No significantly sintering can be observed, indicating the benefits of glycine-nitrate combustion method in synthesis of perovskite materials, like reducing the synthesis temperature, remaining relatively fine and average particles, and avoiding some impurity phases. The high resolution transmission electron microscopy (HRTEM) image in Fig. 2(b) shows the detail microstructure of LSFT sample. The lattice spacing of LSFT sample is 0.2769 nm, which is close to the lattice spacing (0.2766 nm) of (110) plane in the cubic crystal system with a space group of $Pm\bar{3}m$, shown in Table 1. It means that this result also keeps consistent with the XRD analysis. Considering some trace amount of elements are difficult to be detected by XRD, the LSFT sample is further examined by an EDX. As shown in Fig. 2(c), apart from the original elements of La, Sr, Fe and Ti, there is no any other impurity elements exist in the LSFT sample. At the meantime, the atomic proportion of La: Sr: Fe: Ti is 0.36: 0.72: 0.10: 0.86, which comes close to the theoretical atomic ratio of 0.30: 0.70: 0.10: 0.90.

The near-surface composition and the elements valence state of the samples are examined using XPS analysis. The full range XPS spectra for both of LST and LSFT can be found in the supporting information (Fig. S2). From the full range XPS spectra, no significant change can be found for La, Sr, Ti and O species of LSFT sample, comparing to that of LST sample, while a weak Fe peak arises in the range of 700-740 eV for the LSFT sample. Furthermore, Fig. 3(a) and Fig. 3(b) are expanded regions

XPS spectra in the 450-470 eV and 526-534 eV ranges for Ti and O species of LST and LSFT, respectively. As shown in Fig. 3(a), the peak located at 457.57 eV can be attributed to Ti^{3+} $2P_{3/2}$ valence state, while the Ti^{4+} $2P_{3/2}$ peak locates at 458.06 with additional satellite peak at 463.58 eV. Previous reports of XPS analysis of the O 1s region of perovskites show two main features assigned to the surface and lattice oxygens [40-42]. As shown in Fig.3(b), the fitted O 1s spectra display two major oxygen XPS peaks centered at 529.11 eV and 530.86 eV. The first band can be attributed to the lattice oxygen (O^{2-}), and the second band is attributed to the surface-active oxygen (O_2^{2-}/O^-). The surface concentrations ratios of Ti^{3+} and O_2^{2-}/O^- for LST and LSFT are given in Table 2. Obviously, both of Ti^{3+} and O_2^{2-}/O^- species increase after doping Fe into the LST. It is reported that the perovskite oxide's surface property is critically related to the generation of oxygen active species, and the amount of intermediate oxygen species derived from the activation of oxygen such as O_2^{2-} or O^- are responsible for the catalytic performance of perovskite oxides in CO oxidation [43, 44]. O_2^{2-}/O^- species are strongly electrophilic reactants, which attack the CO molecule in the region of its highest electron density, resulting an easier association of CO and dissociation of O_2^{2-}/O^- species. It is generally accepted that a perovskite material with higher concentration of surface-active oxygen (O_2^{2-}/O^-) might possess more amounts of active oxygen defects [45-49], which might benefit the electrooxidation of CO occurred at the surface of the perovskite materials. For the XPS analysis on the near-surface composition of LST before and after reduction, Zhu et al. and Luo et al. have reported

similar results. Zhu et al. reported that the amount of the surface oxygen species in the LST powder after reduction in H_2 increased slightly compared to that in the raw powder, but increased significantly in the LST after the fuel cell measurement in H_2/air conditions [50]. This phenomenon was attributed to the phase transition of LST, which were partially crystallized and widened amorphous layers with large amounts of oxygen vacancies and become the ion fast conduction channels of LST electrolytes. Luo et al. found that the binding energy spectra of all elements in the Co-doped LST remained almost unchanged, but the peak intensity of all the component elements decreased after treatment in 5000 ppm H_2S-H_2 [51]. These results demonstrate the superiority and chemical stability of LST and doped LST.

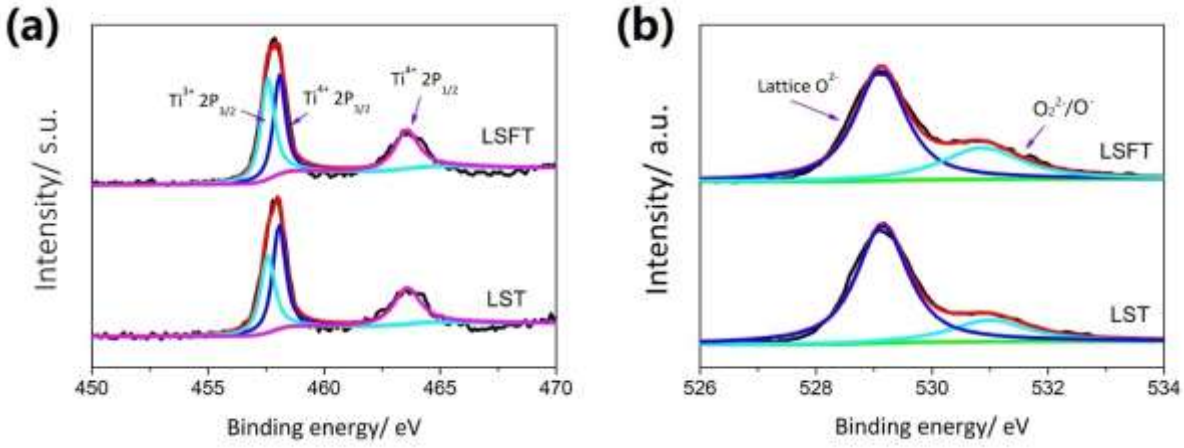

Fig. 3. High resolution XPS spectra of LST and LSFT: (a) Ti 2P spectra and (b) O 1S spectra.

Table 2

Surface concentration of Ti and O species for LST and LSFT samples

	Ti^{3+}	Ti^{4+}	O_2^{2-}/O^-	O^{2-}
LST	45.5%	54.5%	21.2%	78.8%
LSFT	53.5%	46.5%	30.6%	69.4%

2. Electrochemical measurement

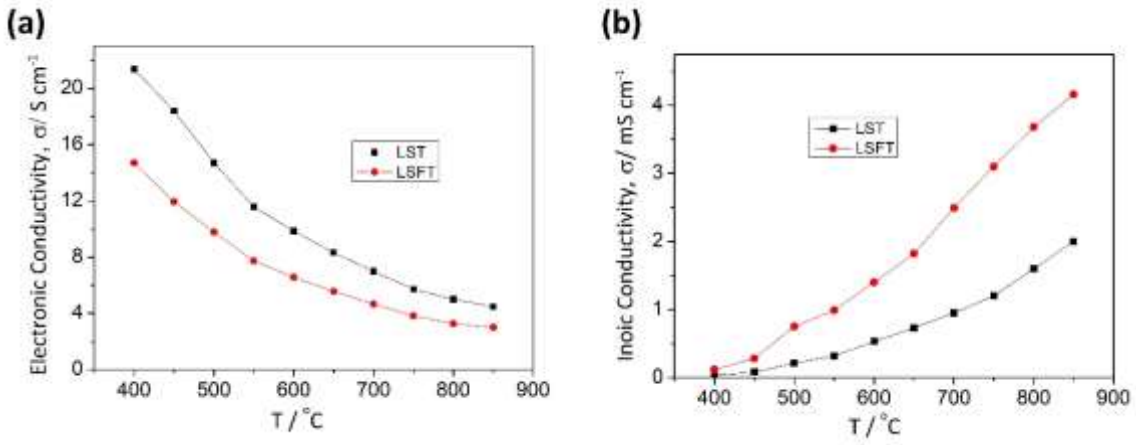

Fig. 4. Electronic conductivity (a) and ionic conductivity (b) of LST and LSFT measured in CO-CO_2 mixed gases atmosphere in the temperature range of 400-850 ºC.

High electronic and ionic conductivities are the basic requirements for an excellent electrode of SOFCs. The variations of electronic and ionic conductivities of LST and LSFT with respect to temperature (400-850 °C) are shown in Fig. 4(a). The electronic conductivity test was performed in a CO-CO_2 mixed gases atmosphere (95 % CO, 5 % CO_2) to simulate the anode atmosphere of DC-SOFC using a four-probe DC technique. While, the ionic conductivity test was measured by electron-blocking method in CO-CO_2 mixed gases atmosphere. Fig. 4(a) shows the electronic conductivities of LST and LSFT decrease with temperature, indicating the titanate anodes behave like a metallic-type behavior in CO-CO_2 mixed gases atmosphere.

However, the electronic conductivity of LST reduces from 5.0 S cm^{-1} to 3.3 S cm^{-1} at 850 °C after doping Fe element, which is also reported by Li and Zhao [52], doping different content of Co in $La_{0.3}Sr_{0.7}TiO_3$ in forming gas atmosphere (5 *vol*% hydrogen in argon). High electronic conductivity is absolutely desirable for SOFC anode. Nevertheless, if the electrode microstructure is optimized, a relatively low electrical conductivity of 1 S cm^{-1} is still acceptable. In comparison to LST, the ionic conductivity of LSFT is remarkably higher at the temperature range of 400-850 °C. As shown in Fig. 4(b), the ionic conductivity of LST is only 2.0 mS/cm at 850 °C, comparing to 6.2 mS/cm for LSFT. For perovskite oxides, the oxygen ionic conductivity primarily depends on oxygen vacancy concentrations at a certain temperature and carrier mobility referring to B–O interactions between metal and lattice oxygen ion and the geometrical factor of lattice structure. Compared to Ti^{4+} ions, the Fe^{4+} ions tend to be reduced easily to Fe^{3+} ions at high temperatures, accompanying with the formation of corresponding amount of oxygen ion vacancies. Considering the electrostatic neutrality, there is an equilibrium between the concentrations of defects existing in $La_{0.3}Sr_{0.7}Fe_{0.1}Ti_{0.9}O_3$:

$$[La_{Sr}^{\cdot}] + 2[V_o^{\cdot\cdot}] = [Fe_{Ti}'] + [Ti_{Ti}']$$

Doping Fe will increase the oxygen vacancy concentration but decrease the Ti^{3+} concentration. At high temperature, the increased oxygen vacancy concentration leads to the increased ionic conductivity, while the decreased Ti^{3+} concentration results in the decreased electronic conductivity.

In solid-state physics, electronic band theory can be used to describe the general

characteristics of the internal motion of electrons in solids. The electronic band structure (or simply band structure) of a solid describes the range of energy levels that electrons may have within it, as well as the ranges of energy that they may not have, called band gaps or forbidden bands. Band theory derives these bands and band gaps by examining the allowed quantum mechanical wave functions for an electron in a large, periodic lattice of atoms or molecules [53]. According to electronic band theory, a band gap can be referred to the energy difference between the bottom of the conduction band and the top of the valence band. After doping Fe, the valence band of LST might move away from the conduction band edge, which results in a wider band gap of LST system and worse electronic conductivity. For stoichiometric LST, interstitial oxygen is always existed in crystal lattice. While, if it exposes to a reducing atmosphere, the interstitial oxygen would remove from the LST crystal lattice and leads to an increased amount of Ti^{3+} and oxygen vacancy, which improves the ionic conductivity [54]. As it is well known, the activation energy for oxygen ion migration (E_a) is the barrier energy which must be provided to an oxygen ion to result in migration, indicating the sensitivity of the reaction rate or migration rate to temperature. Therefore, the activation energy for oxygen ion migration calculated by Arrhenius equation is shown in Fig. 5. It is found that the E_a for oxygen ion migration of LSFT (0.97 eV) is lower than that of LST (1.03 eV), meaning that Fe-doping facilitates the oxygen ion conduction.

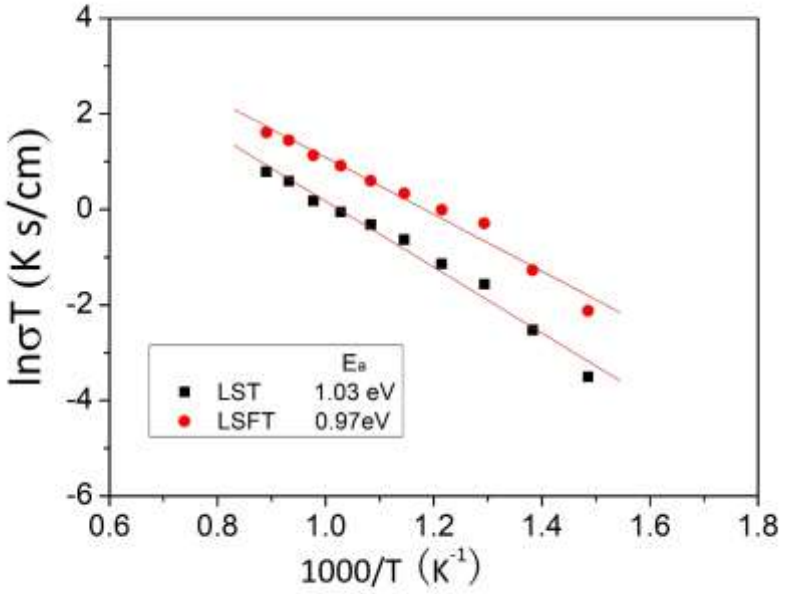

Fig. 5. Arrhenius-type plots of the ionic conductivity and activated energy (E_a) for LST and LSFT measured in the CO-CO_2 mixed gases atmosphere.

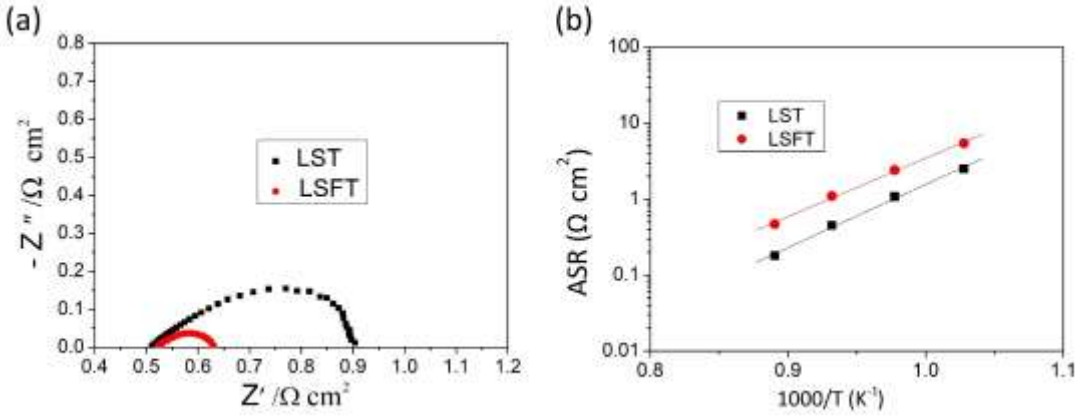

Fig. 6. Impedance spectra (a) and Arrhenius-type plots (b) of symmetric cells with LST-GDC/YSZ/LST-GDC and LSFT-GDC/YSZ/LSFT-GDC configurations in CO-CO_2 mixed gases atmosphere, respectively.

Apart from the electronic and ionic conductivities, electrocatalytic activity is also an essential nature for an anode material of SOFC. Fig. 6 shows typical EIS (Fig. 6a) and the Arrhenius-type plots of area-specific resistances (Fig.6b) for both LST-GDC/YSZ/LST-GDC and LSFT-GDC/YSZ/LSFT-GDC symmetric cells in the CO-CO_2 mixed gases atmosphere at various temperatures respectively. The high-frequency intercepts with the real axis in the Nyquist plot, associated with the ohmic resistances, are almost the same for both cells. However, the polarization resistance of LSFT based symmetric cell is about 0.11 Ω cm^{-2} at 850 °C, which is significantly lower than that of LST based symmetric cell (0.40 Ω cm^{-2}). A lower electrode polarization resistance reflects a higher catalytic activity for electrochemical reaction on the anode. The disillusioned output performance of LST anode SOFC is caused by the poor electrocatalytic activity of LST toward the oxidation of fuel gases, including hydrogen and methane. In previous studies, doping transition metal (cobalt, iron, manganese, nickel) on B-site of LST perovskite oxide is found to be an effective way to improve the electrocatalytic activity of LST and even output performance of an LST anode SOFC operated on hydrogen or methane as fuel [55, 56]. Similarly, in our study, the LSFT perovskite material exhibits lower ASRs than that of the iron-free LST (Fig. 6b), which suggests a superior electrocatalytic activity of LSFT under the operating condition of DC-SOFC.

The electrochemical performances of the LST and LSFT SOFC are evaluated using humidified hydrogen (3 vol.% H_2O) as fuel. The thickness of YSZ electrolyte is

about 200 μm while the anode has a thickness of 25 μm (Fig. S4). As shown in Fig. S5, an open circuit voltage of 1.05 V is obtained for both LST cell and LSFT cell, indicating the YSZ electrolyte is dense. The LSFT cell delivered a peak power density of 351 mW cm^{-2} at 850 °C, which is much higher than that of LST cell (286 mW cm^{-2}). Although this output performance is not impressive, it is acceptable for an electrolyte-supported SOFC, as ohmic resistance of the thick electrolyte dominates the total resistance of the cell.

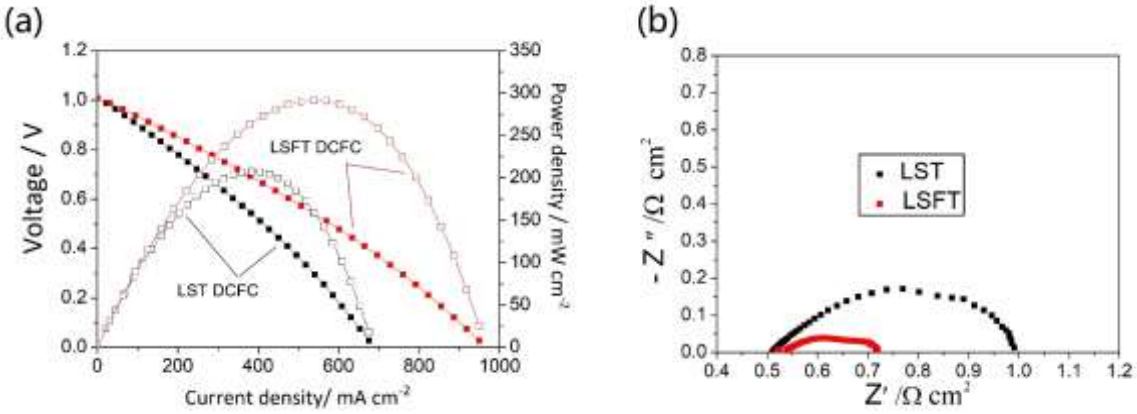

Fig. 7. Cell output performances and impedance spectra of LST and LSFT anode DC-SOFCs at 850 ºC.

The electrochemical performances of the LST and LSFT are further evaluated as the anodes of DC-SOFC. It has been reported that the output performance of a DC-SOFC can be effectively enhanced through loading Ca catalyst on the carbon fuel to promote the Boudouard reaction rate [16]. Therefore, in this work, 5 wt. % Ca-loaded activated carbon is used as the carbon fuel for DC-SOFCs. In addition, a DC-SOFC is more suitable to operate at high temperature above 850 °C, as CO is the favor product

instead of CO_2 at high temperature in a C-O system with excess amount of carbon. Moreover, limited to the practical conditions, we use silver wires as current wires in this experiment, and the melting point of silver is only about 960 °C. Accordingly, we just compare the output performances of the cells at 850 °C. As can be seen from Fig. 7(a), the LSFT DC-SOFC gives a maximum power density of 292 mW cm^{-2}, which is lower than that operated on humidified hydrogen (351 mW cm^{-2}) and obviously higher than that of LST DC-SOFC (207 mW cm^{-2}). Both of the open circuit voltages are about 1.01 V. At the same time, the electrochemical impedance spectra of the DC-SOFCs measured at open circuit voltage are shown in Fig. 7(b). The ohmic resistances of the two cells are also similar, due to the same YSZ electrolyte thickness and operating temperature. However, the polarization resistances of the cells are different, which is consistently with the results of the symmetric cells. It further demonstrates the preferable electrocatalytic activity of LSFT for the electrooxidation of CO, comparing to that of LST. Such performances are comparable to those obtained for other DC-SOFCs with typical anode materials like Ni-YSZ, Ag-GDC and LSFN, and substantially higher than those of cells with electrolyte support configuration (Table 3).

Table 3

Output performance comparison of DC-SOFCs with different anode materials.

Anode	Supporter type	Temperature / °C	Carbon fuel	Performance / mW cm^{-2}
Ni-YSZ [2]	Anode	850	Fe-activated carbon	424
Ni-YSZ [57, 58]	Electrolyte	800	De-ash coal	127
Ni-Cu-YSZ [17]	Electrolyte	800	Carbon+ CO_2	118
SFM-LSGM [18]	Electrode	850	Fe-activated carbon	405
Ag-GDC [4]	Electrolyte	850	Leaf char	212
Ag-LSCF [59]	Electrolyte	800	Carbon+ CO_2	64
LSCT [34]	Electrolyte	800	Carbon black	25
LSFN [19]	Electrolyte	850	Activated carbon	302.8
LSFT-GDC (This work)	Electrolyte	850	Ca-activated carbon	292

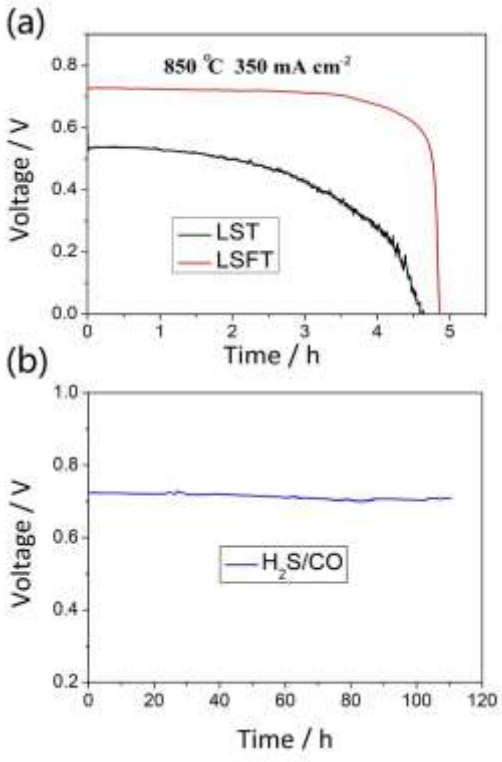

Fig. 8. The discharging curves (a) of LST and LSFT anode DC-SOFCs powered by 0.4 g of Ca-loaded activated carbon, and the long-term stability (b) of LSFT anode cell operated on CO with high contents of H_2S (1000 ppm) at 850 ºC.

Shown in Fig. 8(a) is the discharging curve of the DC-SOFC with LSFT anode, operated at 0.4 g Ca-loaded activated carbon as fuel. The cell operates at 850 °C, maintained at a constant current of 350 mA cm^{-2}. The discharging time of the cell is about 4.8 h. Similar to the previous work, the LSFT DC-SOFC shows a stable discharging platform, and then abruptly drop to 0 V. It can be attributed to the consumption of carbon fuel and decline of the Boudouard reaction [16]. Limited by the capacity of anode chamber of DC-SOFCs, the amount of Ca-loaded activated carbon is not enough to support a long-term operation for DC-SOFC. In other words, the stability of the anode material of DC-SOFC can not be effectively assessed, if the discharging test for DC-SOFC only remains for several hours. Actually, the fixed-bed DC-SOFC system can be improved and realize a continuous fuel feed and long term discharging operation, which is reported by Lü et. al. [60]. However, in this case, a long-term operation also can be achieved using external gas supply instead of solid carbon fuel. As we have mentioned above, the reactant involved in the electrochemical reaction on the anode of DC-SOFCs is CO, which is produced by the Boudouard reaction on the carbon fuel. It means, to a certain extent, the electrochemical behaviors of a SOFC operated on external CO gas can be deemed to the same as a DC-SOFC, which has been verified in our previous work [12]. For another, considering the practical application of DC-SOFC, the most common carbon fuels in real life are coal and biomass carbon, which contain sulfur more or less. Therefore, in this work, we use H_2S/CO (H_2S, 1000 ppm) as fuel to supply the cell to evaluate the stability of LSFT anode. Fig. 7(b) shows

the long-term stability of the cell operated on H_2S/CO at 850 °C, maintained at a constant current density of 350 mA cm^{-2}. The discharge voltage of the cell remains almost unchanged for about 110 hours, which demonstrates the high stability of LSFT for an anode of DC-SOFCs. The excellent sulfur tolerance of LST anode has been systematically studied by Luo et. al. [51], which supports the stability of LSFT anode in this work.

4. Conclusions

A small substitution of Ti in $La_{0.3}Sr_{0.7}TiO_3$ with Fe, results in enhanced ionic conductivity and electrocatalytic activity of the perovskite oxide with stable face-centered cubic lattice structure. The relative low polarization resistance in CO-CO_2 mixed gases atmosphere and high output performance of the corresponding DC-SOFC is demonstrated. Electrolyte-supported DC-SOFCs with LSFT anode provides a peak power density of 292 mW cm^{-2} at 850 °C, which is comparable to those state-of-the-art Ni-YSZ anode for DC-SOFC. The increased electronic conductivity and enhanced concentration of surface-active oxygen (O_2^{2-}/O^-) of LSFT might be the main reasons for the improved electrochemical performances. Furthermore, a DC-SOFC with LSFT anode shows excellent sulfur tolerant ability, as it stably discharges for over 110 hours with H_2S/CO (1000 ppm) as fuel. The high electrochemical performance together with the excellent stability in H_2S-containing CO demonstrates that LSFT is a promising anode candidate for DC-SOFC with whole-solid-state configuration.

Acknowledgements

This work was supported by the National Science Foundation of China (NSFC, No. 91745203 and U1601207), the Special Funds of Guangdong Province Public Research and Ability Construction (No. 2014A010106008), Science and Technology Program of Guangdong Province (No.2017B010122001). M. Ni thanks the grant (Project Number: PolyU 152214/17E and PolyU 152064/18E) from Research Grant Council, University Grants Committee, Hong Kong SAR.

References

[1] Wu W, Zhang Y, Ding D, He T. A High-Performing Direct Carbon Fuel Cell with a 3D Architectured Anode Operated Below 600° C. Adv. Mater. 2018;30:1704745.

[2] Bai Y, Liu Y, Tang Y, Xie Y, Liu J. Direct carbon solid oxide fuel cell—a potential high performance battery. Int. J. Hydrogen Energy 2011;36:9189-94.

[3] Tang Y, Liu J. Effect of anode and Boudouard reaction catalysts on the performance of direct carbon solid oxide fuel cells. Int. J. Hydrogen Energy 2010;35:11188-93.

[4] Cai W, Zhou Q, Xie Y, Liu J, Long G, Cheng S, Liu M. A direct carbon solid oxide fuel cell operated on a plant derived biofuel with natural catalyst. Appl. Energy 2016;179:1232-41.

[5] Kupecki J, Skrzypkiewicz M, Motylinski K. Variant analysis of the efficiency of

industrial scale power station based on DC-SOFCs and DC-MCFCs. Energy 2018;156:292-8.

[6] Liu Q, Tian Y, Xia C, Thompson LT, Liang B, Li Y. Modeling and simulation of a single direct carbon fuel cell. J. Power Sources 2008;185:1022-9.

[7] Rady AC, Giddey S, Kulkarni A, Badwal SPS, Bhattacharya S, Ladewig BP. Direct carbon fuel cell operation on brown coal. Appl. Energy 2014;120:56-64.

[8] Liu J, Zhou M, Zhang Y, Liu P, Liu Z, Xie Y, Cai W, Yu F, Zhou Q, Wang X. Electrochemical oxidation of carbon at high temperature: principles and applications. Energy fuel. 2017;32:4107-17.

[9] Xie Y, Cai W, Xiao J, Tang Y, Liu J, Liu M. Electrochemical gas–electricity cogeneration through direct carbon solid oxide fuel cells. J. Power Sources 2015;277:1-8.

[10] Cao D, Sun Y, Wang G. Direct carbon fuel cell: fundamentals and recent developments. J. Power Sources 2007;167:250-7.

[11] Nakagawa N, Ishida M. Performance of an internal direct-oxidation carbon fuel cell and its evaluation by graphic exergy analysis. Ind. Eng. Chem. Res. 1988;27:1181-5.

[12] Xie Y, Tang Y, Liu J. A verification of the reaction mechanism of direct carbon solid oxide fuel cells. J. Solid State Electrochem. 2013;17:121-7.

[13] Wang C, Lü Z, Su C, Li J, Cao Z, Zhu X, Wu Y, Li H. Effects of discharge mode and fuel treating temperature on the fuel utilization of direct carbon solid oxide fuel cell.

Int. J. Hydrogen Energy 2019;44:1174-81.

[14] Jiao Y, Tian W, Chen H, Shi H, Yang B, Li C, Shao Z, Zhu Z, Li S-D. In situ catalyzed Boudouard reaction of coal char for solid oxide-based carbon fuel cells with improved performance. Appl. Energy 2015;141:200-8.

[15] Wu Y, Su C, Zhang C, Ran R, Shao Z. A new carbon fuel cell with high power output by integrating with in situ catalytic reverse Boudouard reaction. Electrochem. Commun. 2009;11:1265-8.

[16] Cai W, Liu J, Yu F, Zhou Q, Zhang Y, Wang X, Liu M, Ni M. A high performance direct carbon solid oxide fuel cell fueled by Ca-loaded activated carbon. Int. J. Hydrogen Energy 2017;42:21167-76.

[17] Tomov R, Dudek M, Hopkins S, Krauz M, Wang H, Wang C, Shi Y, Tomczyk P, Glowacki B. Inkjet Printing of Direct Carbon Solid Oxide Fuel Cell Components. ECS Transac. 2013;57:1359-69.

[18] Xiao J, Han D, Yu F, Zhang L, Liu J, Zhan Z, Zhang Y, Dong P. Characterization of symmetrical $SrFe_{0.75}Mo_{0.25}O_{3-\delta}$ electrodes in direct carbon solid oxide fuel cells. J. Alloys Compd. 2016;688:939-45.

[19] Li J, Wei B, Wang C, Zhou Z, Lü Z. High-performance and stable $La_{0.8}Sr_{0.2}Fe_{0.9}Nb_{0.1}O_{3-\delta}$ anode for direct carbon solid oxide fuel cells fueled by activated carbon and corn straw derived carbon. Int. J. Hydrogen Energy 2018;43(27):12358-67.

[20] Zhou X, Yan N, Chuang KT, Luo J. Progress in La-doped $SrTiO_3$ (LST)-based anode materials for solid oxide fuel cells. RSC Adv. 2014;4:118-31.

[21] Cowin PI, Petit CT, Lan R, Irvine JT, Tao S. Recent progress in the development of anode materials for solid oxide fuel cells. Adv. Energy Mater. 2011;1:314-32.

[22] Savaniu C, Irvine J. La-doped $SrTiO_3$ as anode material for IT-SOFC. Solid State Ionics 2011;192:491-3.

[23] Neagu D, Irvine JTS. Structure and Properties of $La_{0.4}Sr_{0.4}TiO_3$ Ceramics for Use as Anode Materials in Solid Oxide Fuel Cells. Chem. Mater. 2010;22:5042-53.

[24] Hu Q, Liu C, Fan L, Wang Y, Xiong Y. Nanofiber-based La0.4Sr0.6TiO 3-Gd0.2Ce0.8O1.9-Ni composite anode for solid oxide fuel cells. Electrochim. Acta 2018;265:1-9.

[25] Shao L, Si F, Fu X-Z, Luo J-L. Archiving high-performance solid oxide fuel cells with titanate anode in sulfur- and carbon-containing fuels. Electrochim. Acta 2018;270:9-13.

[26] Savaniu C-D, Irvine JT. Reduction studies and evaluation of surface modified A-site deficient La-doped $SrTiO_3$ as anode material for IT-SOFCs. J. Mater. Chem. 2009;19:8119-28.

[27] Ovalle A, Ruiz-Morales JC, Canales-Vázquez J, Marrero-López D, Irvine JT. Mn-substituted titanates as efficient anodes for direct methane SOFCs. Solid State Ionics 2006;177:1997-2003.

[28] Verbraeken MC, Ramos T, Agersted K, Ma Q, Savaniu CD, Sudireddy BR, Irvine JTS, Holtappels P, Tietz F. Modified strontium titanates: from defect chemistry to SOFC anodes. RSC Adv. 2015;5:1168-80.

[29] Miller DN, Irvine JTS. B-site doping of lanthanum strontium titanate for solid oxide fuel cell anodes. J. Power Sources 2011;196:7323-7.

[30] Yoon H, Zou L, Sammes NM, Chung J. Ru-doped lanthanum strontium titanates for the anode of solid oxide fuel cells. Int. J. Hydrogen Energy 2015;40:10985-93.

[31] Li X, Zhao H, Zhou X, Xu N, Xie Z, Chen N. Electrical conductivity and structural stability of La-doped $SrTiO_3$ with A-site deficiency as anode materials for solid oxide fuel cells. Int. J. Hydrogen Energy 2010;35:7913-8.

[32] Gan Y, Qin Q, Chen S, Wang Y, Dong D, Xie K, Wu Y. Composite cathode $La_{0.4}Sr_{0.4}TiO_{3-\delta}$–$Ce_{0.8}Sm_{0.2}O_{2-\delta}$ impregnated with Ni for high-temperature steam electrolysis. J. Power Sources 2014;245:245-55.

[33] Park BH, Choi GM. Electrochemical performance and stability of $La_{0.2}Sr_{0.8}Ti_{0.9}Ni_{0.1}O_{3-\delta}$ and $La_{0.2}Sr_{0.8}Ti_{0.9}Ni_{0.1}O_{3-\delta}$ - $Gd_{0.2}Ce_{0.8}O_{2-\delta}$ anode with anode interlayer in H_2 and CH_4. Electrochim. Acta 2015;182:39-46.

[34] Kulkarni A, Giddey S, Badwal S, Paul G. Electrochemical performance of direct carbon fuel cells with titanate anodes. Electrochim. Acta 2014;121:34-43.

[35] Dong F, Chen D, Chen Y, Zhao Q, Shao Z. La-doped $BaFeO_{3-delta}$ perovskite as a cobalt-free oxygen reduction electrode for solid oxide fuel cells with oxygen-ion conducting electrolyte. J. Mater. Chem. 2012;22:15071-9.

[36] Lu J, Li S, Tao S, Zhang T, Xie K. Efficient CO2 electrolysis with scandium doped titanate cathode. Int. J. Hydrogen Energy 2017;42:8197-206.

[37] Cai W, Liu J, Xie Y, Xiao J, Liu M. An investigation on the kinetics of direct carbon

solid oxide fuel cells. J. Solid State Electrochem. 2016;20:2207-16.

[38] Liu S, Behnamian Y, Chuang KT, Liu Q, Luo J-L. A-site deficient La0. 2Sr0. 7TiO3− δ anode material for proton conducting ethane fuel cell to cogenerate ethylene and electricity. J. Power Sources 2015;298:23-9.

[39] Bartel CJ, Sutton C, Goldsmith BR, Ouyang R, Musgrave CB, Ghiringhelli LM, Scheffler M. New tolerance factor to predict the stability of perovskite oxides and halides. Science advances 2019;5:eaav0693.

[40] Hong WT, Stoerzinger KA, Crumlin EJ, Mutoro E, Jeen H, Lee HN, Shao-Horn Y. Near-Ambient Pressure XPS of High-Temperature Surface Chemistry in Sr2Co2O5 Thin Films. Top. Catal. 2016;59:574-82.

[41] Crumlin EJ, Mutoro E, Liu Z, Grass ME, Biegalski MD, Lee Y-L, Morgan D, Christen HM, Bluhm H, Shao-Horn Y. Surface strontium enrichment on highly active perovskites for oxygen electrocatalysis in solid oxide fuel cells. Energy & Environmental Science 2012;5:6081-8.

[42] Van Der Heide P. Systematic x-ray photoelectron spectroscopic study of La1− xSrx-based perovskite-type oxides. Surface and Interface Analysis: An International Journal devoted to the development and application of techniques for the analysis of surfaces, interfaces and thin films 2002;33:414-25.

[43] Sun S, Yang L, Pang G, Feng S. Surface properties of Mg doped LaCoO3 particles with large surface areas and their enhanced catalytic activity for CO oxidation. Applied Catalysis A: General 2011;401:199-203.

[44] Yang J, Hu S, Fang Y, Hoang S, Li L, Yang W, Liang Z, Wu J, Hu J, Xiao W, Pan C, Luo Z, Ding J, Zhang L, Guo Y. Oxygen Vacancy Promoted O2 Activation over Perovskite Oxide for Low-Temperature CO Oxidation. ACS Catalysis 2019;9:9751-63.

[45] Bloed C, Vuong J, Enriquez A, Raghavan S, Tran I, Derakhshan S, Tavassol H. Oxygen Vacancy and Chemical Ordering Control Oxygen Evolution Activity of Sr2–x Ca x Fe2O6− δ Perovskites. ACS Applied Energy Materials 2019;2:6140-5.

[46] Klasen A, Baumli P, Sheng Q, Johannes E, Bretschneider SA, Hermes IM, Bergmann VW, Gort C, Axt A, Weber SA. Removal of Surface Oxygen Vacancies Increases Conductance Through TiO2 Thin Films for Perovskite Solar Cells. The Journal of Physical Chemistry C 2019;123:13458-66.

[47] Cheng Y, Raman AS, Paige J, Zhang L, Sun D, Chen MU, Vojvodic A, Gorte RJ, Vohs JM. Enhancing oxygen exchange activity by tailoring perovskite surfaces. The journal of physical chemistry letters 2019;10:4082-8.

[48] Yang J, Hu S, Fang Y, Hoang S, Li L, Yang W, Liang Z, Wu J, Hu J, Xiao W. Oxygen vacancy promoted O2 activation over perovskite oxide for low-temperature CO oxidation. ACS Catalysis 2019;9:9751-63.

[49] Bao S, Ma C, Chen G, Xu X, Enriquez E, Chen C, Zhang Y, Bettis JL, Whangbo M-H, Dong C. Ultrafast atomic layer-by-layer oxygen vacancy-exchange diffusion in double-perovskite LnBaCo 2 O 5.5+ δ thin films. Scientific reports 2014;4:1-5.

[50] Chen G, Zhu B, Deng H, Luo Y, Sun W, Liu H, Zhang W, Wang X, Qian Y, Hu X. Advanced fuel cell based on perovskite La–SrTiO3 semiconductor as the electrolyte

with superoxide-ion conduction. ACS applied materials & interfaces 2018;10:33179-86.

[51] Yan N, Zanna S, Klein LH, Roushanafshar M, Amirkhiz BS, Zeng Y, Rothenberg G, Marcus P, Luo J-L. The surface evolution of $La_{0.4}Sr_{0.6}TiO_{3+\delta}$ anode in solid oxide fuel cells: Understanding the sulfur-promotion effect. J. Power Sources 2017;343:127-34.

[52] Li X, Zhao H, Xu N, Zhou X, Zhang C, Chen N. Electrical conduction behavior of La, Co co-doped $SrTiO_3$ perovskite as anode material for solid oxide fuel cells. Int. J. Hydrogen Energy 2009;34:6407-14.

[53] Kittel C, McEuen P, McEuen P. *Introduction to solid state physics*: Wiley New York; 1996.

[54] Burnat D, Heel A, Holzer L, Kata D, Lis J, Graule T. Synthesis and performance of A-site deficient lanthanum-doped strontium titanate by nanoparticle based spray pyrolysis. J. Power Sources 2012;201:26-36.

[55] Yoo KB, Park BH, Choi GM. Stability and performance of SOFC with SrTiO3-based anode in CH4 fuel. Solid State Ionics 2012;225:104-7.

[56] Kim JH, Miller D, Schlegl H, McGrouther D, Irvine JT. Investigation of microstructural and electrochemical properties of impregnated (La, Sr)(Ti, Mn) O3±δ as a potential anode material in high-temperature solid oxide fuel cells. Chem. Mater. 2011;23:3841-7.

[57] Dudek M. On the utilization of coal samples in direct carbon solid oxide fuel cell

technology. Solid State Ionics 2015;271:121-7.

[58] Dudek M, Tomczyk P, Socha R, Hamaguchi M. Use of ash-free “Hyper-coal” as a fuel for a direct carbon fuel cell with solid oxide electrolyte. Int. J. Hydrogen Energy 2014;39:12386-94.

[59] Giddey S, Kulkarni A, Munnings C, Badwal SPS. Composite anodes for improved performance of a direct carbon fuel cell. J. Power Sources 2015;284:122-9.

[60] Zhu X, Li Y, Lü Z. Continuous conversion of biomass wastes in a $La_{0.75}Sr_{0.25}Cr_{0.5}Mn_{0.5}O_{3-\delta}$ based carbon–air battery. Int. J. Hydrogen Energy 2016;41:5057-62.